Optically thick winds of very massive stars
suppress intermediate-mass black hole formation

Stefano Torniamenti[1,2], [ID] ⋆, Michela Mapelli[2,3,4,5] [ID] ⋆⋆, Lumen Boco[2] [ID] ⋆⋆⋆,

Filippo Simonato[4,6,7], Giuliano Iorio[8] [ID], Erika Korb[4,2]

[1] Max-Planck-Institut für Astronomie, Königstuhl 17, 69117, Heidelberg, Germany
[2] Universität Heidelberg, Zentrum für Astronomie (ZAH), Institut für Theoretische Astrophysik, Albert Ueberle Str. 2, 69120, Heidelberg, Germany
[3] Universität Heidelberg, Interdiszipliäres Zentrum für Wissenschaftliches Rechnen, D-69120 Heidelberg, Germany
[4] Dipartimento di Fisica e Astronomia Galileo Galilei, Università di Padova, Vicolo dell'Osservatorio 3, I–35122 Padova, Italy
[5] INFN, Sezione di Padova, Via Marzolo 8, I–35131 Padova, Italy
[6] Gran Sasso Science Institute (GSSI), Viale Francesco Crispi 7, 67100 L'Aquila, Italy
[7] INFN, Laboratori Nazionali del Gran Sasso, 67100 Assergi, Italy
[8] Departament de Física Quàntica i Astrofísica, Institut de Ciències del Cosmos, Universitat de Barcelona, Martí i Franquès 1, E-08028 Barcelona, Spain

ABSTRACT

Intermediate-mass black holes (IMBHs) are the link between stellar-mass and supermassive black holes. Gravitational waves have started unveiling a population of IMBHs in the $\sim 100-300\,\mathrm{M}_\odot$ range. Here, we investigate the formation of IMBHs from very massive stars (VMSs, $> 100\,\mathrm{M}_\odot$). We calculate new VMS models that account for the transition from optically thin to optically thick winds, and study how this enhanced mass loss affects IMBH formation and the black hole mass function at intermediate and high metallicity ($Z = 10^{-4} - 0.02$). We show that optically thick winds suppress the formation of IMBHs from direct VMS collapse at metallicities $Z > 0.001$, one order of magnitude lower than predicted by previous models. Our models indicate that the stellar progenitors of GW231123 must have had a metallicity $Z < 0.002$, if the primary black hole formed via direct VMS collapse.

Key words. stars: massive – stars: black holes – stars: mass loss

1. Introduction

Intermediate-mass black holes (IMBHs), with masses $M_{\mathrm{BH}} \sim 10^2 - 10^5\,\mathrm{M}_\odot$ are the link between stellar-mass and supermassive black holes at the center of galaxies (Greene et al. 2020). In the last few years, gravitational waves have provided the first compelling evidence of their existence. The merger remnant of GW190521 represents the first IMBH ever detected via gravitational waves, with a mass of $142^{+28}_{-16}\,\mathrm{M}_\odot$ (Abbott et al. 2020; Abbott et al. 2020). More recently, parameter estimation for the event GW231123 (The LIGO Scientific Collaboration et al. 2025c) reveals a black hole (BH) remnant with $m \sim 240\,\mathrm{M}_\odot$. Both BBH components of GW231123 have masses within or above the pair-instability mass gap (Heger & Woosley 2002; Woosley et al. 2007), with peculiarly high spins ($\chi \gtrsim 0.7$) that hint at the dynamical origin of this merger (Gerosa & Berti 2017; Fishbach et al. 2017; Antonini et al. 2019; Gerosa & Fishbach 2021; Mapelli et al. 2021; Antonini et al. 2025). The current fourth gravitational-wave transient catalog (The LIGO Scientific Collaboration et al. 2025a,b) already contains a number of other IMBH candidates, which is expected to increase with the next observing runs.

At the same time, searches for IMBHs in the Milky Way globular clusters have mostly led to inconclusive results (Mezcua 2017), with only a few debated candidate BHs (Miller-Jones et al. 2012; Tremou et al. 2018; Baumgardt et al. 2019). One notable exception is represented by ω Centauri, which hosts an IMBH with mass $\geq 8 \times 10^3\,\mathrm{M}_\odot$, as revealed by proper motions based on over 20 years of HST data (Häberle et al. 2024).

Possible IMBH formation pathways include the direct collapse of very massive stars (VMS), with masses above $100\,\mathrm{M}_\odot$ (Crowther et al. 2010; Bestenlehner et al. 2014; Vink et al. 2015; Costa et al. 2025; Shepherd et al. 2025), stellar collisions in dense young star clusters (Portegies Zwart & McMillan 2002; Freitag et al. 2006b,a; Mapelli 2016; Di Carlo et al. 2021; Torniamenti et al. 2022), and hierarchical BH mergers in dense and massive star clusters (Antonini et al. 2019, 2023; Mapelli et al. 2021; Rizzuto et al. 2021; Arca Sedda et al. 2023; Torniamenti et al. 2024).

VMSs have been observed in star forming regions and young massive clusters (Vink et al. 2015), like the Arches cluster near the Galactic Center (Martins et al. 2008), NGC 3603 (Crowther et al. 2010), and R136 in the Large Magellanic Cloud (LMC, Crowther et al. 2010; Bestenlehner et al. 2014, 2020). The estimated initial masses of these objects are up to $\sim 300\,\mathrm{M}_\odot$ (Crowther et al. 2010). Also, most of them are observed as single stars (Crowther et al. 2010), which may hint that their formation

⋆ sttorniamenti@mpia.de
⋆⋆ mapelli@uni-heidelberg.de
⋆⋆⋆ lumen.boco@uni-heidelberg.de

is triggered or enhanced by stellar collisions during the earliest stellar phases (Portegies Zwart et al. 1999; Mapelli 2016). The possibility that VMSs form IMBHs, however, strongly depends on the amount of mass they lose during their life (Vink 2018).

At solar metallicity, VMSs can lose a large fraction of their initial mass already during the main sequence, and leave relatively low-mass compact objects (< 30 M$_\odot$, Belczynski et al. 2010; Mapelli et al. 2013; Romagnolo et al. 2024). At low metallicity, these stars could preserve enough mass to enter the pair-instability regime (Spera & Mapelli 2017; Renzo et al. 2020). Namely, stars developing He cores in the 64–135 M$_\odot$ range at the end of carbon burning eventually explode as (pair-instability) supernovae leaving no compact remnant (Heger & Woosley 2002; Woosley et al. 2007; Yungelson et al. 2008), whereas stars that develop even more massive He cores efficiently undergo photodisintegration and possibly collapse into IMBHs (Spera & Mapelli 2017). Also, the retention of the envelope can trigger a dredge-up phase during the core helium-burning phase, remove mass from the stellar core and, in turn, prevent pair-production episodes (Costa et al. 2021).

Most current models predict that VMSs can form IMBHs up to metallicities $Z \lesssim 0.014$ (see, e.g., Costa et al. 2025), where stellar winds become strong enough to prevent the formation of stellar cores with > 100 M$_\odot$. Recently, Sabhahit et al. (2022, 2023, hereafter S22; S23) introduced a new model for stellar winds in VMSs based on the concept of transition mass loss (Vink et al. 2011; Vink & Gräfener 2012) to account for the transition from optically thin winds of O-type stars to the optically thick wind regime. This predicts enhanced mass-loss rates ($\dot{M} \gtrsim 10^{-4}$ M$_\odot$) already during the main sequence, when the star is radiation-pressure dominated – i.e., when its luminosity is very close to or even above the Eddington value. In this case, the wind mass-loss rate is strong enough to reduce the core mass (S23). This improved wind implementation has proved to naturally account for the narrow range of observed VMS temperatures in the Galaxy and the LMC (S22). Also, it heavily suppresses the occurrence of pair instability due to lower core masses. In a recent work, we estimate that this new wind formalism can naturally yield rates of pair instability supernovae consistent with observations (Simonato et al. 2025). Another consequence we may naturally expect is the suppression of IMBH production from VMSs in the regime where optically thick winds become effective.

Here, we investigate the formation of IMBHs from VMSs. We account for optically thick winds to assess how different metallicities and mass-loss rates affect the formation of these objects. To this purpose, we have run an extensive set of VMS models with MESA (Paxton et al. 2011, 2018) to explore the impact of stellar winds on the mass of the VMS cores and the resulting BH masses. We find that IMBH formation is strongly suppressed by our optically thick wind model, even at the metallicity of the LMC.

This paper is organized as follows. In Sec. 2 we introduce our models for stars and stellar winds. In Sec. 3, we show the BH mass distributions from single and binary stars in presence of optically thick winds. We summarize our results and conclusion in Sec. 4.

2. Methods

We model the evolution of VMSs with the hydro-static stellar evolution code MESA (version r12115; Paxton et al. 2011, 2013, 2015, 2018, 2019; Jermyn et al. 2023) adopting the radiation-driven wind models by S23. First, we evolve VMSs until the last phases before core collapse. Then, we use the population-synthesis code SEVN (Spera et al. 2019; Mapelli et al. 2020; Iorio et al. 2023) to explore the BH mass distribution of single and binary VMSs with different wind models and to study a population of massive binary stars. In the following, we introduce our initial conditions and model parameters.

2.1. VMS models with MESA

We adopt the same initial set-up as Simonato et al. (2025), based on the wind mass-loss scheme by S22 and S23[1]. This wind model is based on the concept of transition mass loss introduced by Vink & Gräfener (2012): the transition from optically thin to optically thick winds takes place when the Eddington ratio of the star (Γ_{Edd}) exceeds the ratio at the transition point $\Gamma_{\mathrm{Edd,tr}}$. At each iteration, we calculate the mass-loss rate $\dot{M}_{\mathrm{Vink}}$, the escape velocity v_{esc} and the terminal speed v_∞ from the stellar luminosity as described in S23. We use these quantities to calculate the wind efficiency parameter, which determines when the switch occurs:

$$\eta_{\mathrm{Vink}}(L) \equiv \frac{\dot{M}_{\mathrm{Vink}}\, v_\infty}{L/c} = \frac{\eta}{\tau_{F,s}}\left(\frac{v_\infty}{v_{\mathrm{esc}}}\right) = 0.75\left(1 + \frac{v_{\mathrm{esc}}^2}{v_\infty^2}(L)\right)^{-1}, \quad (1)$$

where $\tau_{F,s}$ is the the flux-weighted mean optical depth at the sonic point. In the optically thick regime, the wind mass-loss follows Vink et al. (2011):

$$\dot{M} = \dot{M}_{\mathrm{tr}}\left(\frac{L}{L_{\mathrm{tr}}}\right)^{4.77}\left(\frac{M}{M_{\mathrm{tr}}}\right)^{-3.99}, \quad (2)$$

where $\dot{M}_{\mathrm{tr}}$, L_{tr} and M_{tr} are the mass-loss rate, the luminosity, and the mass at the transition point, respectively. During the main sequence, we use Eq. 2 to describe the wind mass-loss in the optically thick regime. Otherwise, we refer to Vink et al. (2001). In the core He-burning phase, we use Eq. 2 for temperatures between 4×10^3 K and 10^5 K, while for $T < 4 \times 10^3$ K, we use the formalism by de Jager et al. (1988). For $T > 10^5$ K and central hydrogen mass fraction $X_C < 0.01$, we adopt the Wolf-Rayet mass-loss by Sander & Vink (2020).

We model convective mixing with the mixing length theory (Cox & Giuli 1968), adopting a constant mixing-length ratio $\alpha_{\mathrm{MLT}} = 1.5$. We determine the convective boundaries by applying the Ledoux criterion (Ledoux 1947). We use the semiconvective diffusion parameter $\alpha_{\mathrm{SC}} = 1$. We choose the exponential overshooting formalism by Herwig (2000), with efficiency parameter $f_{\mathrm{OV}} = 0.03$, to describe this process above the convective regions.

Finally, we activate the `co_burn` net (parameter `auto_extend_net = true`) after the main sequence to have a complete and extended network for C- and O-burning and α-chains. Following Simonato et al. (2025), we define the core radius of each element as the radius inside which the fraction of the lighter element below $f_X = 10^{-4}$. For example, the helium (carbon) core radius is the radius inside which the mass fraction of H (^{4}He) drops below $f_X = 10^{-4}$ ($f_Y = 10^{-4}$). Our definition is the same as the MIST libraries, and yields an accurate description of the core boundary (Paxton et al. 2011, 2013, 2015; Dotter 2016; Choi et al. 2016).

---

[1] The MESA inlists and run_star_extras files by Sabhahit et al. (2023) are publicly available at this link.
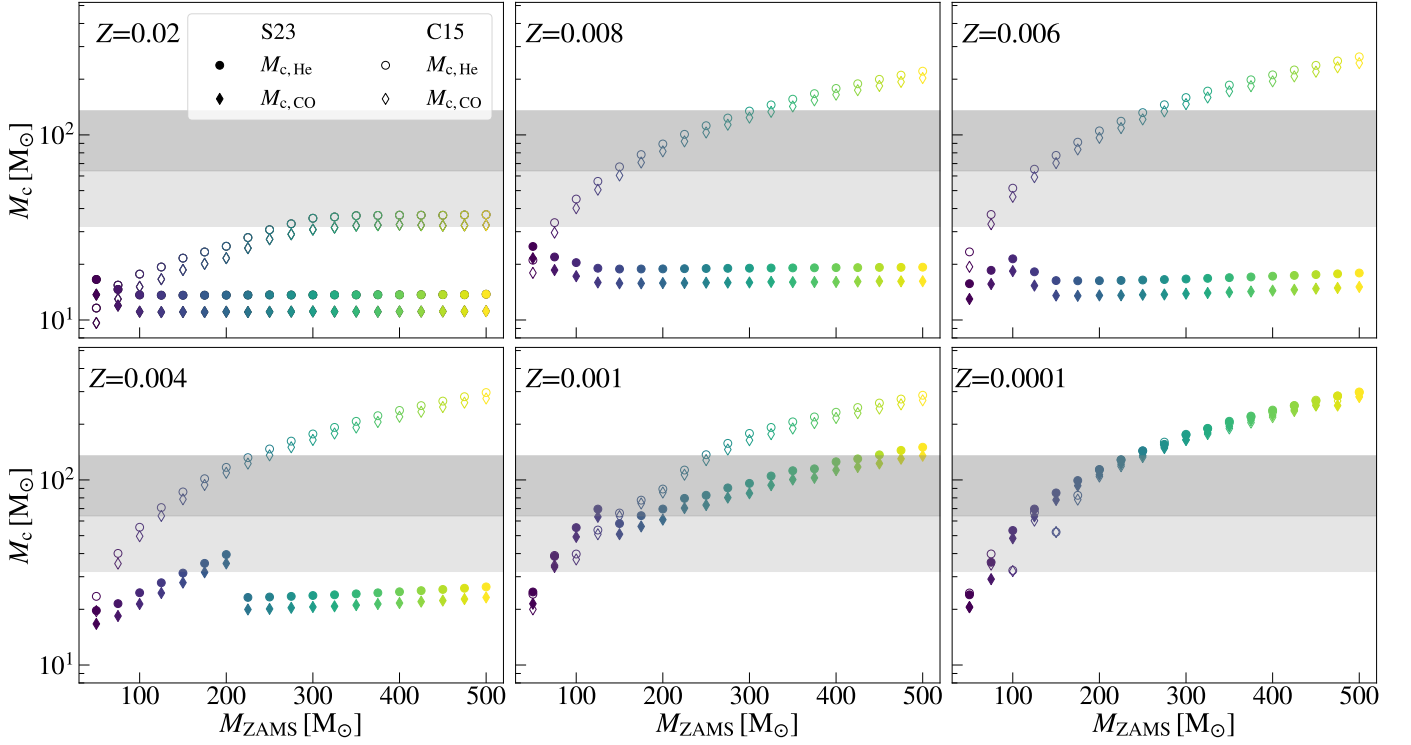
Fig. 1. Masses of the He (circles) and CO cores (diamonds) for the wind model from S23 (full markers) and C15 (void markers). The dark (light) gray shaded areas represent the regime for (pulsational) pair-instability supernovae.

2.2. Initial conditions and stopping criteria

We consider a grid of VMS models with masses from 50 to 500 $M_\odot$, by intervals of 25 $M_\odot$. We consider 14 metallicities from $Z = 10^{-4}$ to $Z = 0.02$. The initial He mass fraction is $Y = Y_{\rm prim} + Z\,\Delta Y/\Delta Z$, with $Y_{\rm prim} = 0.24$ the primordial He abundance and $\Delta Y/\Delta Z$ is parametrized so that we range from a primordial ($Y = 0.24$, $Z = 0$) to nearly a solar abundance ($Y = 0.28$, $Z = 0.02$, Pols et al. 1998). Finally, we calculate the H mass fraction as $X = 1 - Y - Z$. We consider only non-rotating stellar models.

We evolve the MESA models until the star exceeds a central temperature $\log T_c/{\rm K} = 9.55$, corresponding to the very last stages before core collapse, or it undergoes (pulsational) pair-instability. In the latter case, the creation of electron-positron pairs removes thermal pressure from the gas, possibly triggering a state of global dynamical instability. Because we use the hydro-static integrator of MESA, we cannot integrate the models until (pulsational) pair instability kicks in, but we verify a posteriori the global stability of the star. Specifically, we calculate the first adiabatic exponent Γ_1 (e.g., see also Marchant et al. 2019; Farmer et al. 2019, 2020; Costa et al. 2021), properly weighted and integrated over the mass domain (Stothers 1999):

$$\langle \Gamma_1 \rangle = \frac{\int_0^M \frac{P}{\rho} \Gamma_1 \, dm}{\int_0^M \frac{P}{\rho} \, dm}. \tag{3}$$

Here, P is the pressure, ρ is the density and the integral is calculate up to the surface of the star. If a star enters a regime $\langle \Gamma_1 \rangle < 4/3 + 0.01$, we label it as pair-instability and no longer integrate its evolution.

2.3. BH masses

If the star enters the (pulsational) pair-instability regime, we calculate the final BH mass with the fitting formulas from Mapelli et al. (2020), based on the models by Woosley (2017). In this model, a star undergoes a pulsational pair-instability supernova if the He core has a final mass in the range $32\,M_\odot \leq M_{\rm He,f} < 64\,M_\odot$. The mass of the BH is therefore estimated as

$$M_{\rm BH} = \alpha_{\rm P}\,M_{\rm CCSN}, \tag{4}$$

where $M_{\rm CCSN}$ is the expected BH mass after a core-collapse supernova, based on the fitting formulas by Fryer et al. (2012), and $\alpha_{\rm P}$ depends on the mass of He-core and on the ratio between the He-core mass and the total mass in the pre-supernova stage.

If $64\,M_\odot \leq M_{\rm He,f} \leq 135\,M_\odot$, instead, the star undergoes a pair-instability supernova, leaving no compact remnant. If the core mass exceeds $135\,M_\odot$, pair instability triggers photodisintegration and the star directly collapses into a BH, leaving a compact remnant with $M_{\rm BH}$ equal to the total mass of the star.

Mass ejection can also occur in stars that undergo a failed supernova because of the shock triggered by instantaneous neutrino loss (Lovegrove & Woosley 2013; Fernández et al. 2018). The ejected mass depends on the ejected energy and the compactness of the star (Fernández et al. 2018). In particular, the ejected energy is a decreasing function of the core compactness, $\xi_{2.5}$ (O'Connor & Ott 2011). Also, the ejected mass decreases with the stellar envelope compactness, $\xi_{\rm env} = M_*/R_*$, where R_* is the total radius of the star. The ejected mass is a decreasing fraction of $\xi_{\rm env}$ (Fernández et al. 2018), and ranges from $M_{\rm ej} \sim 10\,M_\odot$ for red supergiant stars ($\xi_{\rm env} \sim 10^{-2}$) to $M_{\rm ej} \lesssim 10^{-3}\,M_\odot$ if the star dies as a Wolf-Rayet object ($\xi_{\rm env} \sim 10$).

Following Costa et al. (2022a), we estimate the BH mass for the stars that do not undergo a (pulsational) pair instability
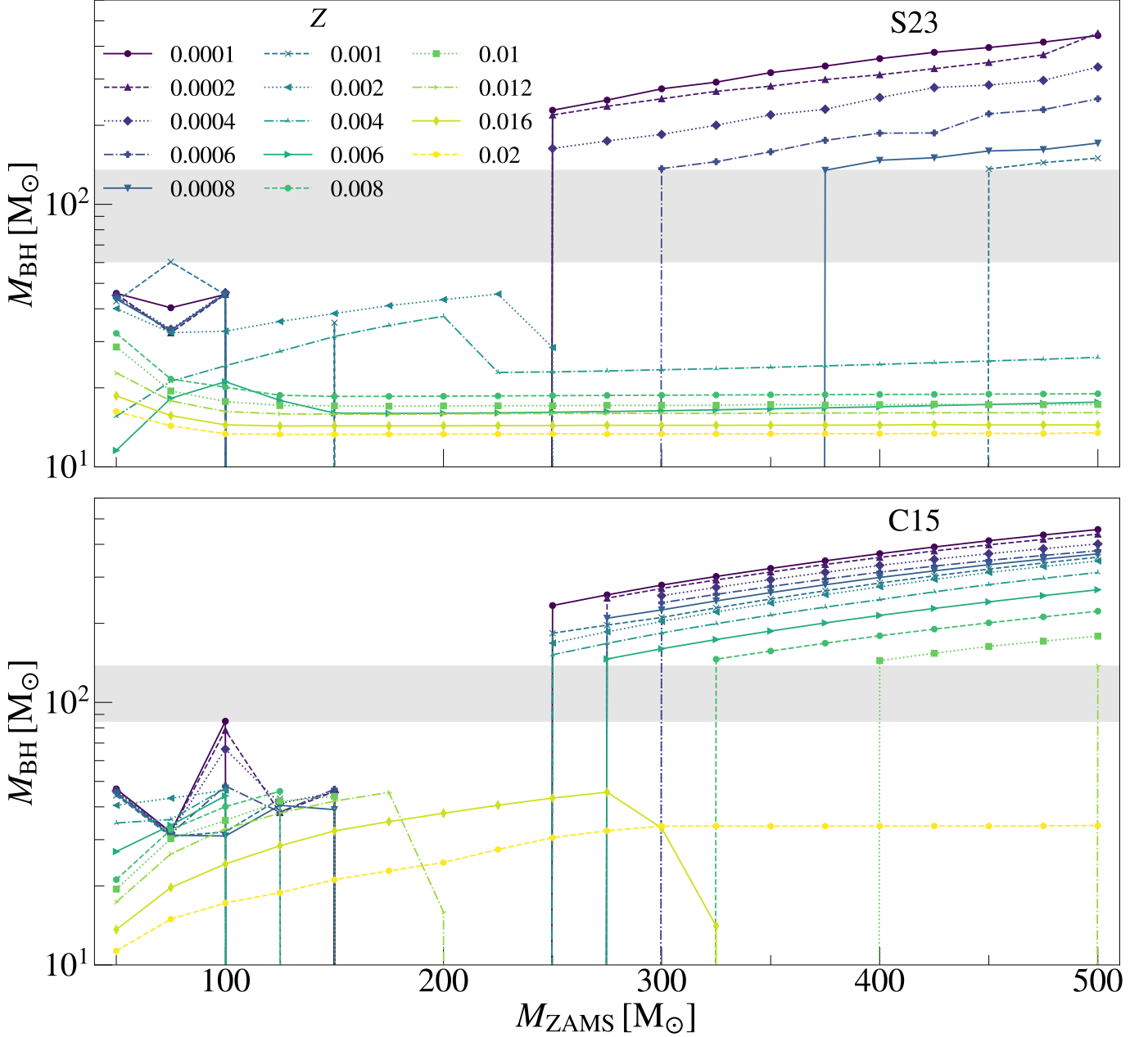
Fig. 2. Final BH mass as a function of M_{ZAMS} for different metallicities Z, for the S23 (upper) and C15 (lower) wind mass-loss prescription. The grey shaded area shows the resulting pair-instability mass gap for the two wind models.

supernova as:

$$M_{\text{BH}} = M_* - \delta M_{\text{G}} - M_{\text{ej}}, \qquad (5)$$

where M_* is the final stellar mass, δM_{G} is the instantaneous gravitational mass loss, and M_{ej} is the the mass induced by neutrino-driven shocks in a failed supernova. Here, we assume $\delta M_{\text{G}} = 0.3\ M_\odot$ (Fernández et al. 2018; Costa et al. 2025), which typically yields a corresponding ejected energy between 10^{47} and 5×10^{47} erg. We thus calculate M_{ej} as the mass of the star with a binding energy less than 3×10^{47} erg.

2.4. Population-synthesis with sevn

We explore the effect of optically thick winds on the mass spectrum of BHs, BBHs and BBH mergers using the population-

synthesis code sevn (Spera & Mapelli 2017; Spera et al. 2019; Mapelli et al. 2020; Iorio et al. 2023)[2]. sevn interpolates pre-computed stellar tracks to evolve single and binary stars. Also, it incorporates semi-analytic formulas for processes like binary mass transfer, tides, supernova explosion, and gravitational-wave decay. We refer to Iorio et al. (2023) for a complete description of the code.

We generate new evolutionary tables for stars with mass $M_\star \geq 50\ M_\odot$ from the aforementioned VMS models with mesa. We then evolve single and binary stars with primary mass in this mass range. For binary stars, we use the stellar tables from par-sec (Bressan et al. 2012; Chen et al. 2015; Costa et al. 2019a,b;

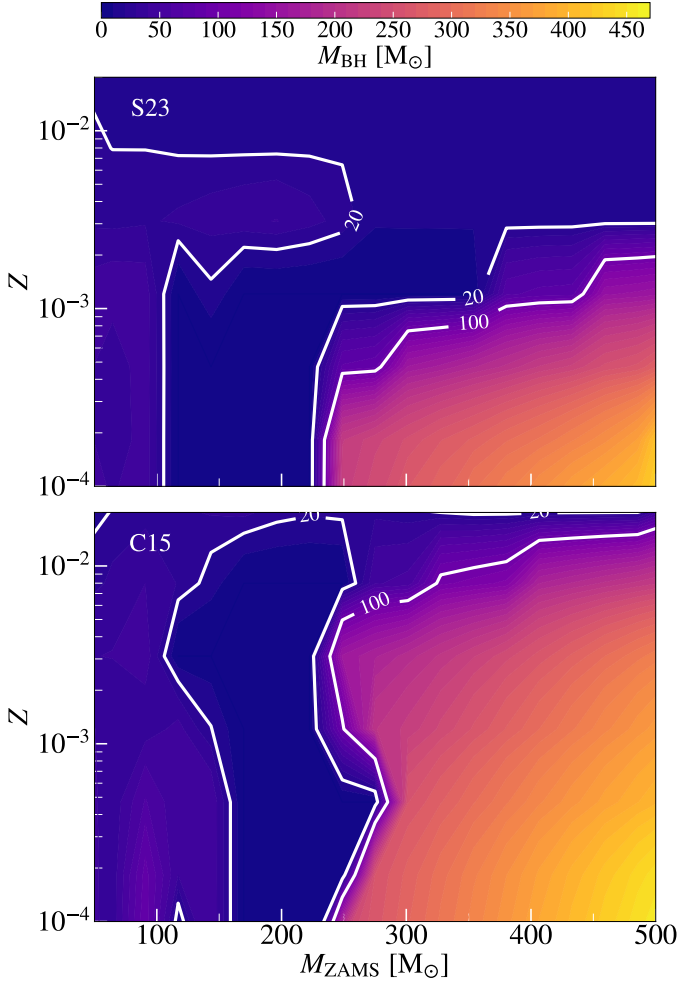[2] We used version 2.10.1 of sevn, updated to commit c9dc8e457. sevn is publicly available here.

Fig. 3. Contour plot showing the final BH mass as a function of M_{ZAMS} and Z, for the S23 (upper panel) and the C15 (lower panel) models. The white contours highlight the levels at $20\,\mathrm{M_\odot}$ and $100\,\mathrm{M_\odot}$.

Nguyen et al. 2022; Costa et al. 2025) to account for the evolution of secondary stars with mass $M_\star < 50\,\mathrm{M_\odot}$.

When two stars collide, we use the standard formalism of sevn as described by Iorio et al. (2023). Specifically, we assume that the collision product retains the total mass of the two stars. The CO and He core masses of the collision product are the sum of the CO and He core masses of the two colliding stars. Finally, the collision product inherits the phase and percentage of life of the most evolved progenitor star. Hence, our models likely overestimate the total mass of the collision product and underestimate mixing. For a more self-consistent treatment of massive star collisions, see, e.g., Costa et al. (2022b) and Ballone et al. (2023).

We randomly draw the zero-age main sequence (ZAMS) primary star masses from a Kroupa (2001) initial mass function, with $M_{\mathrm{ZAMS}} \in [50, 500]$. For binaries, we draw the secondary masses from the observation-based mass ratio distribution $\mathcal{F}(q) \propto q^{-0.1}$, with $q \in [0.1, 1]$ from Sana et al. (2012). We generate the initial orbital periods (P) and eccentricities (e) from the distributions by Sana et al. (2012): $\mathcal{F}(\mathcal{P}) \propto \mathcal{P}^{-0.55}$, with $\mathcal{P} = \log_{10}(P/\mathrm{days}) \in [0.15, 5.5]$ and $\mathcal{F}(e) \propto e^{-0.45}$, with $e \in [10^{-5}, e_{\max}(P)]$, respectively. For a given orbital period, we set the upper limit of the eccentricity distribution $e_{\max}(P)$ as $e_{\max}(P) = 1 - [P/(2\,\mathrm{days})]^{-2/3}$ (Moe & Di Stefano 2017).

We investigate eight different metallicities: $Z = 0.0001$, 0.001, 0.002, 0.004, 0.006, 0.008, 0.01, 0.02. For each metallicity, we generate 2×10^6 single and 1×10^7 binary systems. Our initial setup corresponds to the same as the fiducial model by Iorio et al. (2023). To highlight the impact of stellar winds on the resulting BH mass distribution, we also perform a run with tables from parsec tracks only. In this case, the stellar wind prescription is purely based on the wind model introduced by Chen et al. (2015, hereafter C15), which, in turn is derived from Vink et al. (2000, 2001) for the winds of O-type stars, with additional corrections for electron scattering, the mass-loss dependence on the Eddington ratio (Gräfener & Hamann 2008; Vink et al. 2011). We refer to Simonato et al. (2025) for a thorough comparison between the two wind prescriptions.

3. Results

3.1. Stellar cores

Figure 1 shows the final He and CO core masses for the S23 and C15 wind models. At low metallicity ($Z \leq 0.0001$), the two wind models predict the same monotonic increase of the He and CO core mass with M_{ZAMS}, because VMSs do not enter the optically thick wind regime. At these metallicities, the C15 models generally yield slightly smaller cores, due to the different envelope undershooting and convection models (Simonato et al. 2025).

At higher metallicity, the two considered models C15 and S23 behave in a dramatically different way. According to S23, VMSs can enter the optically thick wind regime at $Z \geq 0.001$: such strong winds reduce the final total mass and core mass of VMSs, resulting in a flat or even decreasing trend of M_c with M_{ZAMS}. Hence, the S23 model predicts smaller He and CO cores compared to C15, with a deep impact on the occurrence of (pulsational) pair instability.

The effect of optically thick winds in the S23 model is twofold. On the one hand, the S23 model results in a lower metallicity threshold below which VMSs can enter the (pulsational) pair instability regime: the threshold is $Z_{\mathrm{th}} = 0.004$ and 0.01 for S23 and C15, respectively. On the other hand, the formation of IMBHs via direct collapse is suppressed in the S23 model for metallicity $Z \geq 0.001$, whereas the C15 model allows the formation of IMBHs already at $Z \leq 0.008$ because of the lower wind mass-loss.

For example, at $Z = 0.001$ optically thick winds become effective for $M_{\mathrm{ZAMS}} > 200\,\mathrm{M_\odot}$, when the stellar core is already well within the pair-instability regime. Mass loss prevents the He core mass from increasing above $135\,\mathrm{M_\odot}$. As a consequence, only VMSs with $M_{\mathrm{ZAMS}} \gtrsim 450\,\mathrm{M_\odot}$ undergo direct collapse to IMBH in the S23 model, whereas in C15 IMBHs can form via direct collapse already at $M_{\mathrm{ZAMS}} \sim 300\,\mathrm{M_\odot}$.

For $Z = 0.004$, VMSs with $M_{\mathrm{ZAMS}} \geq 200\,\mathrm{M_\odot}$ develop stellar winds that are strong enough to reduce the stellar core to $M_c < 30\,\mathrm{M_\odot}$, where even pulsational pair instability is inhibited.

For $Z \gtrsim 0.006$, VMSs in S23 models undergo optically thick stellar winds throughout the mass range considered. This dramatically reduces final core masses, which display a weak dependence on M_{ZAMS}. For example, at $Z \sim 0.006$ the core mass for VMSs with $M_{\mathrm{ZAMS}} > 400\,\mathrm{M_\odot}$ decreases from $\sim 200\,\mathrm{M_\odot}$ in the C15 model to $\sim 20\,\mathrm{M_\odot}$ in S23.

3.2. BH masses

Figure 2 shows the final BH mass as a function of M_{ZAMS} for models C15 and S23. The key difference between the two models

is the metallicity threshold to form IMBHs; this is $Z_{\rm IMBH} = 0.001$ and 0.012 for models S23 and C15, respectively. In model S23, IMBH formation is suppressed at metallicity $Z > 0.001$ by the onset of optically thick winds. These strong winds erode the mass of the He core and prevent it from reaching the threshold $M_{\rm He} \sim 135\,M_\odot$, above which the star avoids to explode as a pair-instability supernova. Thus, even the most massive stars do not produce IMBHs in the S23 model unless they have metallicity $Z \leq 0.001$. In contrast, the lower mass loss in model C15 allows to grow larger cores and enables the formation of IMBHs up to $Z \sim 0.012$.

In absence of optically thick winds, the BH mass increases with $M_{\rm ZAMS}$, up to the onset of (pulsational) pair instability, at $M_{\rm ZAMS} \gtrsim 75\,M_\odot$. For larger initial masses, the onset of direct collapse depends on metallicity. In the C15 model, VMSs undergo (pulsational) pair instability up to $Z = 0.01$. At lower metallicities, all the models with $M_{\rm ZAMS} > 400\,M_\odot$ produce IMBHs, with masses ranging from $135\,M_\odot$ to $450\,M_\odot$. At $Z = 0.02$, instead, wind mass-loss is strong enough to prevent the onset of pair instability, leading to a maximum BH mass $M_{\rm BH} \sim 30\,M_\odot$.

In the S23 model, the maximum metallicity at which IMBHs form is an order of magnitude lower ($Z = 0.001$) compared to C15. Below this threshold, the S23 model produces IMBHs with masses in the same range as C15. At higher metallicities, the most massive BHs originate from stars with $M_{\rm ZAMS} \sim 50 M_\odot$, while more massive stars deliver $M_{\rm BH} \lesssim 15 M_\odot$. This happens because VMSs develop optically thick winds at an early stage, and spend all their lifetime with $\dot{M} > 10^{-5}\,M_\odot\,{\rm yr}^{-1}$. This results in a severe erosion of the core (Simonato et al. 2025; Boco et al. 2025). Overall, the S23 models predict a pair-instability BH mass gap from $65\,M_\odot$ to $135\,M_\odot$.

Figure 3 shows the final BH mass as a function of the ZAMS mass and the metallicity for the S23 model. The formation of IMBHs takes place only for VMSs with $M_{\rm ZAMS} \gtrsim 250\,M_\odot$ at $Z \leq 0.001$. Also, the formation of BHs with $M_{\rm BH} > 20\,M_\odot$ is suppressed for $Z > 0.01$ throughout the mass range.

3.3. BH mass function

3.3.1. BHs from single VMSs

Figure 4 shows the BH mass function from single VMSs assuming a Kroupa (Kroupa 2001) initial mass function. For $Z > 0.001$ optically thick winds strongly suppress the production of IMBHs from single stars. At $Z = 0.001$, the S23 model still allows IMBH formation, but the efficient mass loss limits the maximum BH mass to $150\,M_\odot$, compared to $350\,M_\odot$ in the C15 model. For higher metallicities, stellar winds progressively reduce the maximum BH mass in the S23 model, down to $20\,M_\odot$ at $Z = 0.02$.

In the C15 model, the formation of IMBHs takes place up to $Z = 0.01$, where the maximum BH mass is $\sim 180\,M_\odot$ (see also Costa et al. 2025). At lower metallicities, the maximum IMBH mass reaches $\sim 400\,M_\odot$, for ZAMS masses up to $M_{\rm ZAMS} = 500\,M_\odot$. In this model, IMBH formation from single VMSs is only suppressed at $Z = 0.02$, where BHs can form with a mass up to $33\,M_\odot$.

3.3.2. BBHs from VMS binaries

Figure 5 shows the primary BH masses from binaries with primary mass $M_{\rm ZAMS,1} > 50\,M_\odot$, distributed according to a Kroupa (Kroupa 2001) mass function. We refer to Section 2.4 for more detail on the initial conditions. We display the mass distribution
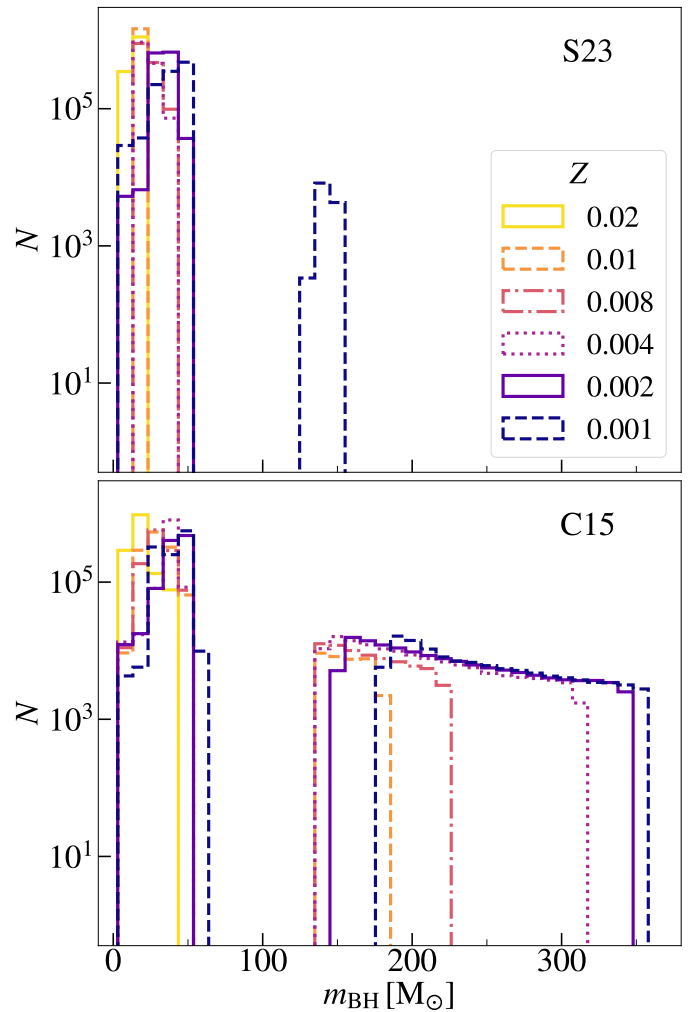

Fig. 4. BH mass distribution from single stars with $M_{\rm ZAMS} > 50\,M_\odot$, for the models adopting the S23 (upper panel) and C15 (lower panel) wind prescriptions and for different metallicities.

of both primary BHs in BBHs and single BHs from disrupted binaries. Star-star collisions dramatically extend the BH mass function to larger values compared to the single stellar-evolution case in Fig. 4.

The C15 model predicts the formation of BHs as massive as $\gtrsim 700\,M_\odot$ for $Z \leq 0.002$. Also, IMBHs up to $\sim 400\,M_\odot$ can still form at $Z = 0.01$. In the S23 model, instead, the formation of IMBHs is suppressed already at $Z = 0.004$, where they represent less than 0.2% of the total BH number, despite the occurrence of star-star colllisions. In contrast, the percentage of IMBHs is 21% in the C15 model at $Z = 0.004$.

Primary BHs in BBHs also reach higher masses than BHs from single stellar evolution, due to mass accretion from the stellar companion. In the S23 model, IMBH formation in BBHs is possible for $Z \leq 0.002$, while for $Z = 0.004$, the maximum primary BH mass in BBHs decreases to $45\,M_\odot$. At $Z = 0.02$, the BH mass function in the S23 model extends from $5\,M_\odot$ to $20\,M_\odot$.

BHs in BBHs display a pair-instability mass gap between $65\,M_\odot$ and $135\,M_\odot$ for both the C15 and the S23 models. In contrast, star-star collisions can produce BHs in this mass range, and fill the pair-instability mass gap with single BHs.
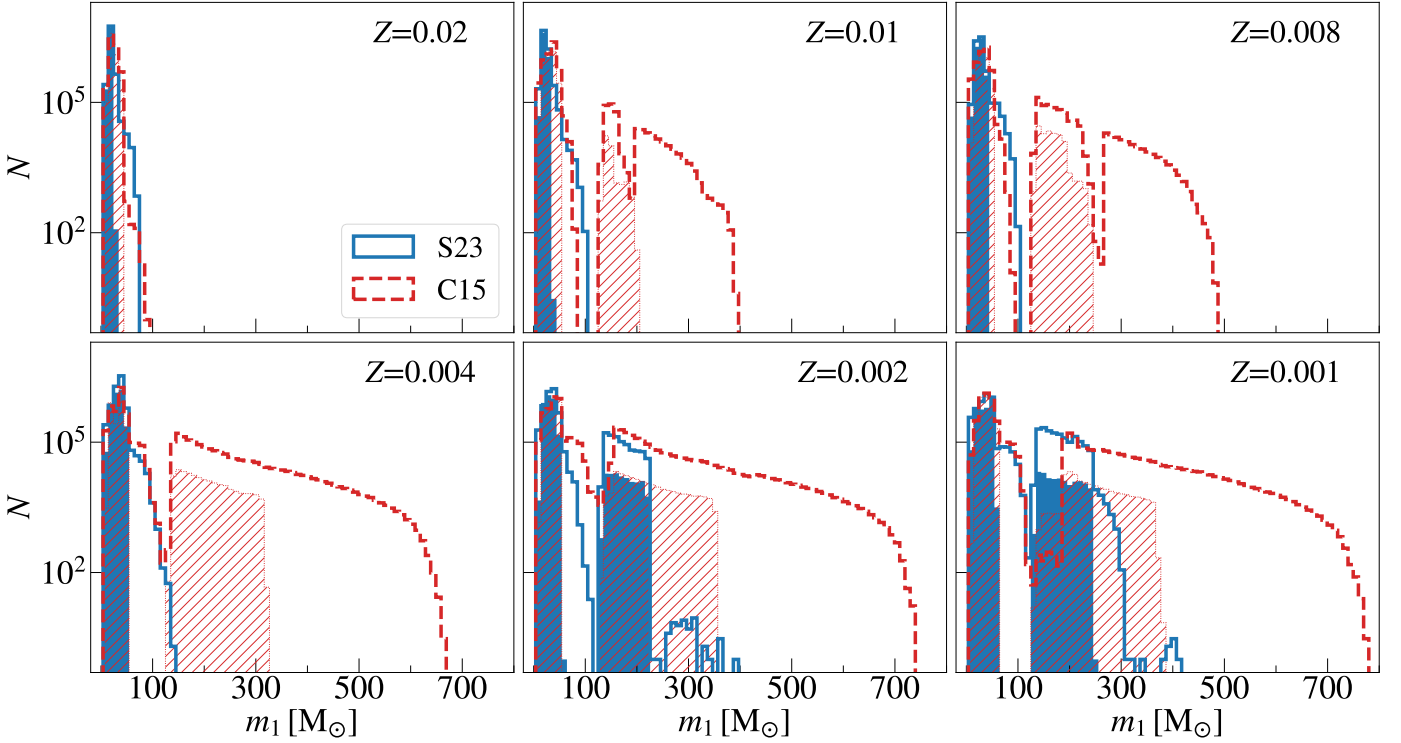
Fig. 5. BH mass distribution from binaries with $M_{ZAMS,1} > 50 M_\odot$, for models adopting the S23 (blue, solid line, solid fill) and C15 (orange, dashed line, hatched area) wind prescriptions. The shaded (hatched) areas indicate the BHs in BBHs, while the empty histograms display the single BHs from disrupted binaries, including BHs that form from stellar collisions.

3.3.3. BBH mergers

Figures 6 and 7 show the primary and remnant mass distributions for BBHs that merge within a Hubble time. In the S23 model, no BBH merger has a primary mass $m_1 > 50 M_\odot$ for $Z > 0.002$. In the C15 case, IMBH mergers can occur up to a metallicity of $Z = 0.004$. In general, the BBH merger mass distribution displays a mild dependence on metallicity, with a peak at $\sim 10 M_\odot$.

The maximum merger remnant produced by these BBHs is usually two times as massive as the maximum primary BH mass. In presence of optically thick winds (model S23), the formation of IMBHs from BBH mergers is thus possible up to $Z = 0.002$, where $m_{BH,max} \sim 240 M_\odot$. At higher metallicities, the maximum BH remnant mass progressively decreases down to $35 M_\odot$ at $Z = 0.02$.

In the C15 models, the masses delivered by BBH mergers are larger, with the possibility of having IMBH remnants up to a metallicity of $Z = 0.006$.

3.3.4. Progenitors of GW231123 and GW190521

We qualitatively compare our models with the most massive BBH mergers detected by the LIGO-Virgo-KAGRA interferometers, namely GW231123 (The LIGO Scientific Collaboration et al. 2025c) and GW190521 (Abbott et al. 2020; Abbott et al. 2020). According to our S23 model, the progenitors of GW231123 should have had a metallicity $Z \leq 0.002$. The primary mass of GW190521 (Abbott et al. 2020; Abbott et al. 2020), instead, lies well within the mass gap predicted by both our C15 and S23 models. In a follow-up work, we will explore the dynamical formation of such mergers with our new S23 models (Torniamenti et al., in prep.).

4. Conclusions

We have investigated the impact of a new optically thick wind model (S23) on the formation of IMBHs in isolated single and binary very massive stars (VMSs). The new model is supported by several observational constraints, such as the pair-instability supernova rate (Simonato et al. 2025) and the existence of single Wolf-Rayet stars at low metallicity (Boco et al. 2025). We have integrated the evolution of VMSs with MESA (Paxton et al. 2019) and have folded our new MESA tracks inside our binary population synthesis code SEVN (Iorio et al. 2023).

We find that IMBH production is suppressed at intermediate metallicity ($Z \in [10^{-3}, 0.01]$), compared to less aggressive wind models. According to our models, IMBHs cannot form from VMS collapse at the metallicity of the LMC ($Z \sim 0.008$) and possibly even the SMC ($Z \sim 0.0025$).

IMBHs might be able to form via stellar collisions at metallicity as high as $Z = 0.004$, but only under the very optimistic assumption that each collision triggers no mass loss. However, even with this assumption for stellar collisions, the occurrence fraction of IMBHs over the total number of BHs ($\lesssim 0.2\%$) is two orders of magnitude lower compared to models with less aggressive winds.

BBH mergers can produce IMBH remnants at metallicity $Z \leq 0.002$. At higher metallicities, the enhanced mass-loss produces BBH mergers with primary mass $m_1 < 50 M_\odot$, making it impossible to form IMBHs from first-generation BH mergers.

The BH mass spectrum from single VMSs shows a pair-instability mass gap from $65 M_\odot$ to $135 M_\odot$. Such mass gap is still present in the mass distribution of BHs in BBHs and BBH mergers.

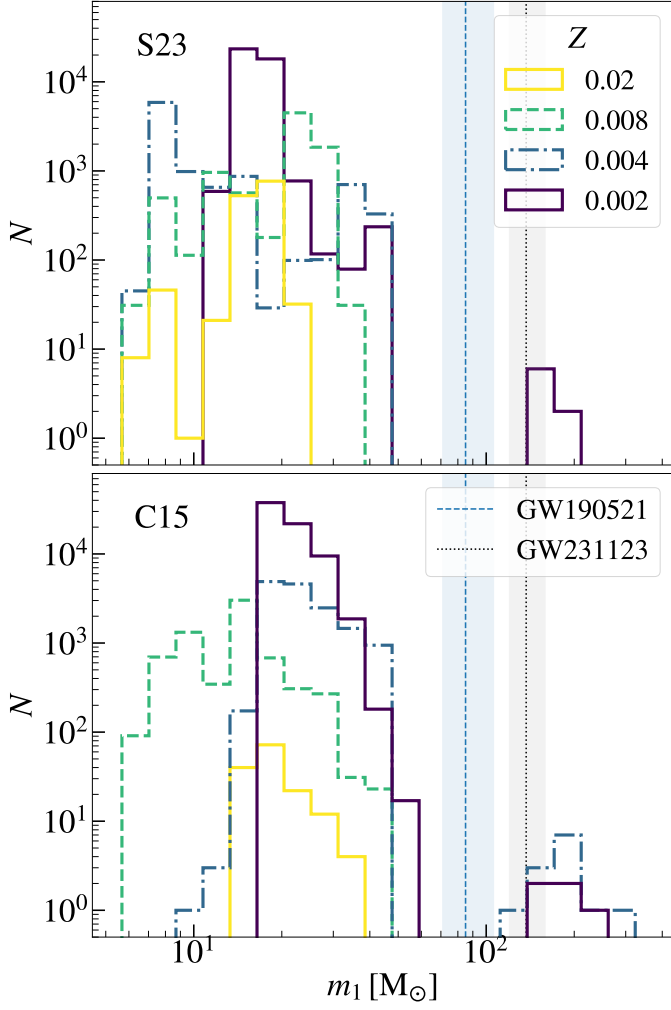According to our S23 models, the progenitors of the most massive BBH observed by the LIGO-Virgo-KAGRA collabo-

Fig. 6. Primary BH mass distribution in BBH mergers with $M_{\rm ZAMS,1} > 50 M_\odot$, for the S23 (upper) and C15 (lower) wind prescriptions, and for different metallicities. The blue dashed (black dotted) line displays the inferred value for GW190521 (GW231123), with the estimated uncertainty (shaded area).
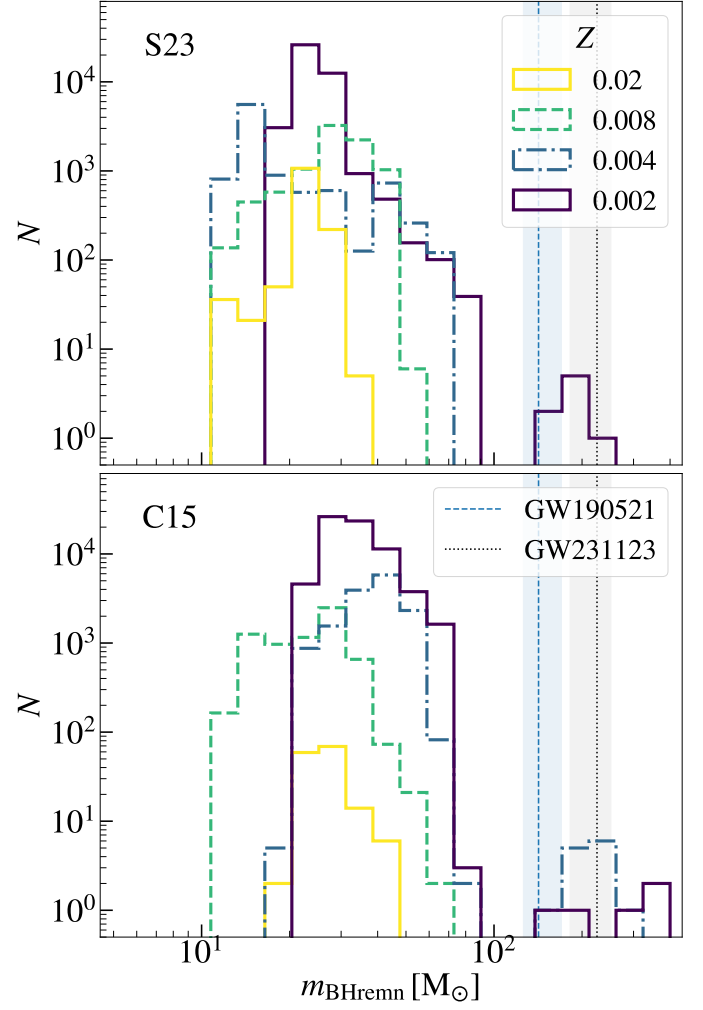
Fig. 7. Same as Fig. 6, but for the resulting BH remnant mass.

(The pandas development Team 2024), SciPy (Virtanen et al. 2020) and Matplotlib (Hunter 2007).

ration, GW231123 (The LIGO Scientific Collaboration et al. 2025c) must have had a metallicity $Z \leq 0.002$. In a follow-up study, we will explore the impact of star cluster dynamics on this result.

References

Abbott, R., Abbott, T. D., Abraham, S., et al. 2020, ApJ, 900, L13

Abbott, R., Abbott, T. D., Abraham, S., et al. 2020, Phys. Rev. Lett., 125, 101102

Antonini, F., Gieles, M., Dosopoulou, F., & Chattopadhyay, D. 2023, MNRAS, 522, 466

Antonini, F., Gieles, M., & Gualandris, A. 2019, MNRAS, 486, 5008

Antonini, F., Romero-Shaw, I., Callister, T., et al. 2025, arXiv e-prints, arXiv:2509.04637

Arca Sedda, M., Kamlah, A. W. H., Spurzem, R., et al. 2023, MNRAS, 526, 429

Ballone, A., Costa, G., Mapelli, M., et al. 2023, MNRAS, 519, 5191

Baumgardt, H., He, C., Sweet, S. M., et al. 2019, MNRAS, 488, 5340

Belczynski, K., Bulik, T., Fryer, C. L., et al. 2010, ApJ, 714, 1217

Bestenlehner, J. M., Crowther, P. A., Caballero-Nieves, S. M., et al. 2020, MNRAS, 499, 1918

Bestenlehner, J. M., Gräfener, G., Vink, J. S., et al. 2014, A&A, 570, A38

Boco, L., Mapelli, M., Sander, A. A. C., et al. 2025, arXiv e-prints, arXiv:2507.00137

Bressan, A., Marigo, P., Girardi, L., et al. 2012, MNRAS, 427, 127

Chen, Y., Bressan, A., Girardi, L., et al. 2015, MNRAS, 452, 1068

Choi, J., Dotter, A., Conroy, C., et al. 2016, ApJ, 823, 102

Costa, G., Ballone, A., Mapelli, M., & Bressan, A. 2022a, MNRAS, 516, 1072

Costa, G., Ballone, A., Mapelli, M., & Bressan, A. 2022b, MNRAS, 516, 1072

Costa, G., Bressan, A., Mapelli, M., et al. 2021, MNRAS, 501, 4514

Costa, G., Girardi, L., Bressan, A., et al. 2019a, A&A, 631, A128

Costa, G., Girardi, L., Bressan, A., et al. 2019b, MNRAS, 485, 4641

Costa, G., Shepherd, K. G., Bressan, A., et al. 2025, A&A, 694, A193

Cox, J. P. & Giuli, R. T. 1968, Principles of stellar structure

Crowther, P. A., Schnurr, O., Hirschi, R., et al. 2010, MNRAS, 408, 731

de Jager, C., Nieuwenhuijden, H., & van der Hucht, K. A. 1988, Bulletin d'Information du Centre de Donnees Stellaires, 35, 141

Di Carlo, U. N., Mapelli, M., Pasquato, M., et al. 2021, MNRAS, 507, 5132

Dotter, A. 2016, ApJS, 222, 8

Farmer, R., Renzo, M., de Mink, S. E., Fishbach, M., & Justham, S. 2020, ApJ, 902, L36

Farmer, R., Renzo, M., de Mink, S. E., Marchant, P., & Justham, S. 2019, ApJ, 887, 53

Fernández, R., Quataert, E., Kashiyama, K., & Coughlin, E. R. 2018, MNRAS, 476, 2366

Fishbach, M., Holz, D. E., & Farr, B. 2017, ApJ, 840, L24

Freitag, M., Gürkan, M. A., & Rasio, F. A. 2006a, MNRAS, 368, 141

Freitag, M., Rasio, F. A., & Baumgardt, H. 2006b, MNRAS, 368, 121

Fryer, C. L., Belczynski, K., Wiktorowicz, G., et al. 2012, ApJ, 749, 91

Gerosa, D. & Berti, E. 2017, Phys. Rev. D, 95, 124046

Gerosa, D. & Fishbach, M. 2021, Nature Astronomy, 5, 749

Gräfener, G. & Hamann, W. R. 2008, A&A, 482, 945

Greene, J. E., Strader, J., & Ho, L. C. 2020, ARA&A, 58, 257

Häberle, M., Neumayer, N., Seth, A., et al. 2024, Nature, 631, 285

Harris, C. R., Millman, K. J., van der Walt, S. J., et al. 2020, Nature, 585, 357

Heger, A. & Woosley, S. E. 2002, ApJ, 567, 532

Herwig, F. 2000, A&A, 360, 952

Hunter, J. D. 2007, Computing in Science and Engineering, 9, 90

Iorio, G., Mapelli, M., Costa, G., et al. 2023, MNRAS, 524, 426

Jermyn, A. S., Bauer, E. B., Schwab, J., et al. 2023, ApJS, 265, 15

Kroupa, P. 2001, MNRAS, 322, 231

Ledoux, P. 1947, ApJ, 105, 305

Lovegrove, E. & Woosley, S. E. 2013, ApJ, 769, 109

Mapelli, M. 2016, MNRAS, 459, 3432

Mapelli, M., Dall'Amico, M., Bouffanais, Y., et al. 2021, MNRAS, 505, 339

Mapelli, M., Spera, M., Montanari, E., et al. 2020, ApJ, 888, 76

Mapelli, M., Zampieri, L., Ripamonti, E., & Bressan, A. 2013, MNRAS, 429, 2298

Marchant, P., Renzo, M., Farmer, R., et al. 2019, ApJ, 882, 36

Martins, F., Hillier, D. J., Paumard, T., et al. 2008, A&A, 478, 219

Mezcua, M. 2017, International Journal of Modern Physics D, 26, 1730021

Miller-Jones, J. C. A., Wrobel, J. M., Sivakoff, G. R., et al. 2012, ApJ, 755, L1

Moe, M. & Di Stefano, R. 2017, ApJS, 230, 15

Nguyen, C. T., Costa, G., Girardi, L., et al. 2022, A&A, 665, A126

O'Connor, E. & Ott, C. D. 2011, ApJ, 730, 70

Paxton, B., Bildsten, L., Dotter, A., et al. 2011, ApJS, 192, 3

Paxton, B., Cantiello, M., Arras, P., et al. 2013, ApJS, 208, 4

Paxton, B., Marchant, P., Schwab, J., et al. 2015, ApJS, 220, 15

Paxton, B., Schwab, J., Bauer, E. B., et al. 2018, ApJS, 234, 34

Paxton, B., Smolec, R., Schwab, J., et al. 2019, ApJS, 243, 10

Pols, O. R., Schröder, K.-P., Hurley, J. R., Tout, C. A., & Eggleton, P. P. 1998, MNRAS, 298, 525

Portegies Zwart, S. F., Makino, J., McMillan, S. L. W., & Hut, P. 1999, A&A, 348, 117

Portegies Zwart, S. F. & McMillan, S. L. W. 2002, ApJ, 576, 899

Renzo, M., Farmer, R. J., Justham, S., et al. 2020, MNRAS, 493, 4333

Rizzuto, F. P., Naab, T., Spurzem, R., et al. 2021, MNRAS, 501, 5257

Romagnolo, A., Gormaz-Matamala, A. C., & Belczynski, K. 2024, ApJ, 964, L23

Sabhahit, G. N., Vink, J. S., Higgins, E. R., & Sander, A. A. C. 2022, MNRAS, 514, 3736

Sabhahit, G. N., Vink, J. S., Sander, A. A. C., & Higgins, E. R. 2023, MNRAS, 524, 1529

Sana, H., de Mink, S. E., de Koter, A., et al. 2012, Science, 337, 444

Sander, A. A. C. & Vink, J. S. 2020, MNRAS, 499, 873

Shepherd, K. G., Costa, G., Ugolini, C., et al. 2025, arXiv e-prints, arXiv:2505.10206

Simonato, F., Torniamenti, S., Mapelli, M., et al. 2025, arXiv e-prints, arXiv:2505.07959

Spera, M. & Mapelli, M. 2017, MNRAS, 470, 4739

Spera, M., Mapelli, M., Giacobbo, N., et al. 2019, MNRAS, 485, 889

Stothers, R. B. 1999, MNRAS, 305, 365

The LIGO Scientific Collaboration, the Virgo Collaboration, & the KAGRA Collaboration. 2025a, arXiv e-prints, arXiv:2508.18083

The LIGO Scientific Collaboration, The Virgo Collaboration, & the KAGRA Collaboration. 2025b, arXiv e-prints, arXiv:2508.18082

The LIGO Scientific Collaboration, the Virgo Collaboration, the KAGRA Collaboration, et al. 2025c, arXiv e-prints, arXiv:2507.08219

The pandas development Team. 2024, pandas-dev/pandas: Pandas

Torniamenti, S., Mapelli, M., Périgois, C., et al. 2024, A&A, 688, A148

Torniamenti, S., Rastello, S., Mapelli, M., et al. 2022, MNRAS, 517, 2953

Tremou, E., Strader, J., Chomiuk, L., et al. 2018, ApJ, 862, 16

Vink, J. S. 2018, A&A, 615, A119

Vink, J. S., de Koter, A., & Lamers, H. J. G. L. M. 2000, A&A, 362, 295

Vink, J. S., de Koter, A., & Lamers, H. J. G. L. M. 2001, A&A, 369, 574

Vink, J. S. & Gräfener, G. 2012, ApJ, 751, L34

Vink, J. S., Heger, A., Krumholz, M. R., et al. 2015, Highlights of Astronomy, 16, 51

Vink, J. S., Muijres, L. E., Anthonisse, B., et al. 2011, A&A, 531, A132

Virtanen, P., Gommers, R., Oliphant, T. E., et al. 2020, Nature Methods, 17, 261

Woosley, S. E. 2017, ApJ, 836, 244

Woosley, S. E., Blinnikov, S., & Heger, A. 2007, Nature, 450, 390

Yungelson, L. R., van den Heuvel, E. P. J., Vink, J. S., Portegies Zwart, S. F., & de Koter, A. 2008, A&A, 477, 223